Bulletin of the Seismological Society of America, Vol. 104, No. 5, pp. –, October 2014, doi: 10.1785/0120130237

A Study of Microseisms Induced by Typhoon Nanmadol Using Ocean-Bottom Seismometers

by Jing-Yi Lin, Tzu-Chuan Lee, Hsin-Sung Hsieh, Yen-Fu Chen, Yi-Chin Lin, Hsin-Hua Lee, and Yi-Ying Wen

Abstract From the end of August to early September 2011, 15 ocean-bottom seismometers (OBSs) were deployed offshore northeastern Taiwan for approximately 20 days. During this period, the typhoon Nanmadol formed in the western Pacific, moved northwestward from the East Philippines, and made landfall on the island of Taiwan. In this study, we analyzed the seismic signals from the OBSs and the marine metrological data to investigate the influence of the typhoon on submarine seismic records. Our results show that the signals induced by the typhoon occurred mainly at approximately 0.15–0.5 Hz frequency. The magnitude of these signals depends substantially on water depth. Some exceptions, most likely generated by site effects, were observed. Also, a positive correlation exists between the signals energy and the local wave height, which suggests that the microseisms were affected by the pressure changes produced by the local wave activity as the typhoon passed over the stations. However, when an OBS was outside the typhoon periphery, any wave energy variations could only be caused by the elastic wave formed around the typhoon area, the energy of which is transmitted through the ocean bottom to the stations. Thus, no local waves were excited by the strong winds, and only a relatively small amount of energy was recorded.

Introduction

Ocean-bottom seismometers (OBSs) have been widely used over the past decades to collect seismic data for seismic monitoring of the ocean floor, exploitation of oil and gas hydrates, and detection of tsunamis. However, OBSs detect more than just earthquakes and active seismic sources. Many other events, such as meteorite impacts and nuclear explosions, can produce distinctive vibrations in the Earth's crust that appear in seismic records. In addition, OBSs are now widely used to observe myriad low-frequency submarine events, such as submarine volcano activity and seafloor monitoring. Among these events, activity in the ocean produces vibrations referred to as microseisms (Longuet-Higgins, 1950; Tabulevich, 1971; Sutton and Barstow, 1990; Kibblewhite and Wu, 1993; Bradley *et al.*, 1997; Suda *et al.*, 1998; Webb, 1998, 2007; Bromirski, 2001; Stephen *et al.*, 2003; Wilson *et al.*, 2003; McNamara and Buland, 2004; Bromirski *et al.*, 2005; Kedar and Webb, 2005; Dahm *et al.*, 2006; Marzorati and Bindi, 2006, 2008; Gerstoft *et al.*, 2008; Koper and de Foy, 2008). These continuous vibrations have two prominent peaks in frequency: 0.05–0.1 Hz (primary or single-frequency [SF] microseisms) and 0.1–0.5 Hz (secondary or double-frequency [DF] microseisms). SF microseisms are generated as ocean waves impact the shore. They are generated only at coastlines and consist of the same range of frequencies that make up ocean surface waves (Hasselmann, 1963). DF microseisms are generated when two waves traveling in opposite directions interact. A nonlinear coupling between the two waves produces a depth-independent oscillation of the water column at twice the frequency of the opposing waves. DF microseisms also can be classified as long-period DF (LPDF, generated by swells) and short-period DF (SPDF, generated by local sea winds) microseisms (Bromirski *et al.*, 2005). The energy and the frequency the microseisms contain are affected by the interaction between the wave and the coast and the wind activity (speed and direction). When ocean waves (swell) are originated from away, the low-frequency ocean waves propagate faster than high-frequency waves. The high-period waves hit the coast before and generate an increase of the frequency content (Bromirski *et al.*, 2005). In addition, as local seas develop, spectral levels are initially highest at short periods, demonstrated by the Pierson–Moskowitz wave model for several wind speeds. As the storm intensifies, the wave energy peak shifts to lower frequencies (longer periods; Bretschneider, 1959).

It has long been recognized that intense cyclonic storms at sea produce strong winds that transfer atmospheric energy into oceanic gravity waves and that part of that energy couples with the solid earth to generate microseisms that propagate in the acoustic system formed by the ocean and solid structure below (Ebeling and Stein, 2011). The propagation

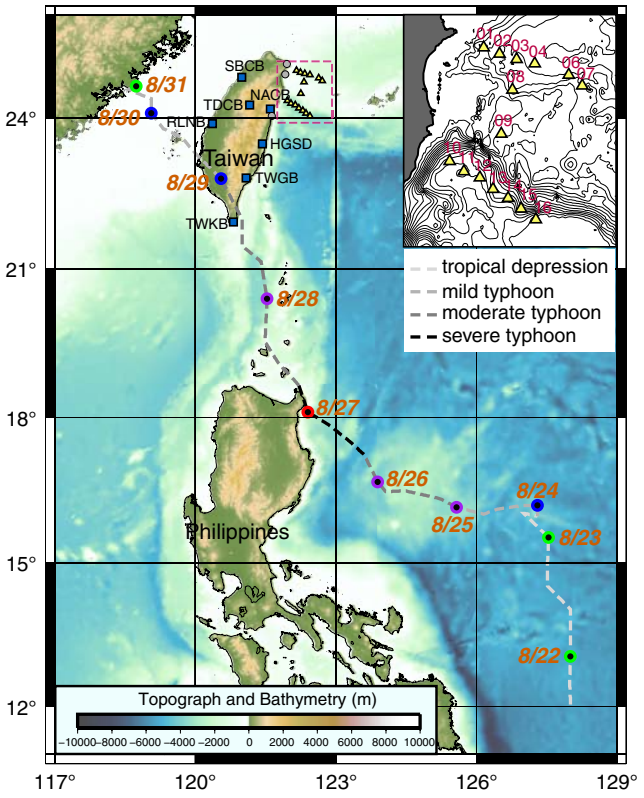

Figure 1. Regional bathymetry with the center track of the typhoon Nanmadol. Triangles show the positions of ocean-bottom seismometers (OBSs), and squares show the positions of the inland broadband stations selected from the Broadband Array in Taiwan for Seismology (BATS) network. The wave buoys are, from north to south, Longdong, Kueishantao, and Hualien, and are indicated by dots. Typhoon intensity is marked by the shading of the dashed lines. The inset shows the configuration of the array of 15 four-component, short-period OBSs. The color version of this figure is available only in the electronic edition.

of microseisms was previously thought to be primarily of the form of Rayleigh waves (Sutton and Barstow, 1990). However, modern array techniques have now allowed observations of significant *P*-wave microseisms that can be associated with sea states (Gerstoft *et al.*, 2008; Koper and de Foy, 2008; Landès *et al.*, 2010). Most analyses regarding these *P*-wave microseisms were performed based on teleseismic data, as direct observations using OBS seismic networks near a typhoon are rare (Chi *et al.*, 2010). In our study, we analyze the waveform data recorded by a temporary seismic network that comprises 15 four-component OBSs located near the path of a passing typhoon. Typhoon Nanmadol was the strongest tropical cyclone to hit the Philippines in 2011 and the first of the year to directly impact Taiwan. It formed on 23 August and reached peak strength with winds of 105 knots (195 km/hr) sustained for 10 min intervals, threatening the Philippines with heavy rain and flash flooding. Nanmadol continued to drift northwest and made landfall in the Philippines on 26 August. Late on 28 August, Nanmadol made landfall in Taiwan. After a tremendous burst of convection over southern Taiwan, land interaction severely weakened the system. Soon, Nanmadol accelerated toward the northwest and entered the Taiwan Strait (Fig. 1). On 31 August, the typhoon was downgraded to a tropical storm. Nanmadol made a total of three landfalls. Comparison among the various data components recorded by different stations provides more information about the origin of the microseisms and the factors affecting the characteristics of the seismic signal. This study has presented an opportunity to illuminate the possible origins of the background noise recorded by the instruments and to improve our data analysis work.

Data Acquisition

Seismic Stations

The Across Taiwan Strait Explosion Experiment (ATSEE) uses seismic techniques to image the crustal and upper mantle structures of the Taiwan mountain belt and its surrounding seas for the purposes of understanding the mountain building processes, plate boundary dynamics, seismogenic mechanisms, and marine geohazards. Two lines on the Taiwan island were also scheduled to measure the structure in northern Taiwan. The OBSs were deployed in both the Taiwan Strait and eastern Taiwan offshore to cover a wider *Pn* range. During this ATSEE 2011 experiment (two cruises: OR2-1812 from 15 to 18 August 2011 and OR2-1817 from 3 to 7 September 2011), 16 short-period OBSs were deployed by the research vessel Ocean Research 2 offshore of northeast Taiwan (Fig. 1; see Data and Resources). Most OBSs are distributed along two east–west profiles. Each profile comprises seven OBSs with approximately 10 km spacing. The northern profile is located along the Okinawa trough, and the southern profile runs along its fore-arc basin. In addition, two OBSs are located on the Ryukyu arc, between the two profiles (Fig. 1). However, one OBS (OBS05) was not recovered successfully (Fig. 1). Both the Okinawa trough and the fore-arc basin have low-lying terrain, and the canyon nearby can bring sediments. The OBS used in the experiment is MicrOBS Plus, an instrument developed by the French Research Institute for Exploitation of the Sea (Ifremer), weighing less than 32 kg and packaged within a 17″ glass sphere, which includes the electronics, the batteries, and the geophones (Geospace GS-11D), and was designed to be deployed offboard the operating vessel (Table 1). All OBSs were equipped with three-component 4.5 Hz geophones and one broadband-type hydrophone (Auffret *et al.*, 2004). After the OBSs are deployed to the seabed, the signals are collected by the OBS sensors, time stamped, and stored in a compact flash memory card. When the experiment is over, an encoded acoustic signal is sent from the ship to the OBS, which releases the anchor weight used to sink the instrument to the bottom of the ocean, and the OBS rises to the surface due to its structural floatability. The OBS clock is synchronized with a Global Positioning System signal prior to its deployment, and clock time drift is calculated after OBS recovery by using the same signal. Based on laboratory results

Table 1
Technical Specifications of the Ocean Bottom Seismometers Used for This Study

Characteristics	Components		Specifications
Weight	MicrOBS	In air	36 kg
		In water	−12.5 kg
	MicrOBS + dead weight	In air	64 kg
		In water	11.5 kg
Sensors	Configuration	Hydrophone	1 channel
		Geophone	3 axis
	Low-frequency cutoff	Hydrophone	2 Hz (−3 dB)
	Natural frequency	Geophone	4.5 Hz
	Sensitivity	Hydrophone	−160 dB ref 1 V/μPa
		Geophone	32 V/m/s
Batteries	Type		Rechargeable Li-ion 15 V/40 Ah
	Autonomy		8 day idle +24 days acquisition
Memory	Type		Compact flash card 8 GB (optional 16 GB)
	Autonomy		24 day (@2 ms SR)
Dimensions	Base		550 × 550 mm
	Height		720 mm
	Dead weight size (cross shape)		800 × 800 mm
Data logger	Seismic channel		4

obtained in comparable pressure and temperature conditions, linear corrections were applied to the data time mark correction.

In our study, we also use broadband seismic data from selected stations of the Broadband Array in Taiwan for Seismology (BATS) network (see Data and Resources) for comparative waveform and spectral analysis. The broadband seismic observation network (BATS) in Taiwan was established by the Central Weather Bureau (CWB), the broadband seismic observation network of Institute of Earth Sciences, Academia Sinica, and the National Central University, including 32 CWB broadband ground stations, 3 deep-well stations, and 21 broadband stations of IESAS in a total of 56 stations at present. The data collected by such stations are transmitted by the digital network cable of Chunghwa Telecom back to the CWB broadband data processing center. All permanent stations are equipped with state-of-the-art very broadband (Streckeisen STS-1 or STS-2) and strong-motion (Terra Technology SSA-320) sensors and 24-bit digital recorders (Quanterra Q-680 or Q-4120). Data streams with high sampling rates (≥80 samples per second) are recorded in triggering mode, whereas others are recorded in continuous mode on both hard disks and magnetic tapes. All stations are capable of telecommunication for immediate retrieval of specific events.

For further analysis of the seismic data, the instrument response was corrected and the amplitudes were converted to be in displacement for the inland broadband stations. However, no available response curve can be used for the OBS instrument correction. Thus, to convert the OBS data from digital counts to the actual measurement in velocity, we used the formula shown as follows:

$$\text{Amplitude}\left(\text{in}\,\frac{\text{m}}{\text{s}}\right) = \frac{\text{digital counts} \times \text{constant of the data logger}}{10^{\frac{\text{gain}}{20}} \times 1000 \times \text{sensitivity}},$$

in which the gain is set to be 32 during the operation, the sensitivity is 32 V/(m/s), and the constant of the data logger is 2500/6291455. Even though the approximate amplitudes in meters per second can be obtained for the OBS data by using the formula, it should not be appropriate to compare the amplitude of OBS and inland data directly due to the different signal amplification in different frequency ranges. The short-period OBS has a smaller amplification factor for the signal in the low-frequency domain compared to the inland broadband stations. Consequently, discussion in regard to amplitudes and signal energy would only be applied based on the same type of instrument in this study.

Marine Buoys

To get more meteorological and oceanographic data in Taiwan waters, CWB has been corporate with Coastal Ocean Monitoring Center of the National Chengkung University since 1994 to develop an operational data buoy observing system. Data measured and reported from the data buoy include water temperature, wave height, and dominant wave period. Raw data is processed and can be logged onboard the buoy. Only some preprocessed data and parameters are automatically transmitted to the ground receiving station every two hours at assigned times by radio telemetry and immediately relayed to CWB via the Intranet or Internet. Three data buoys around Taiwan, Lungdong, Suao, and Hwalien are available for comparison study in this paper (Fig. 1).

Results

Time Domain

To obtain the waveform characteristics, we first perform a visual inspection of the raw waveform data recorded by the three-component geophones and the hydrophone during the

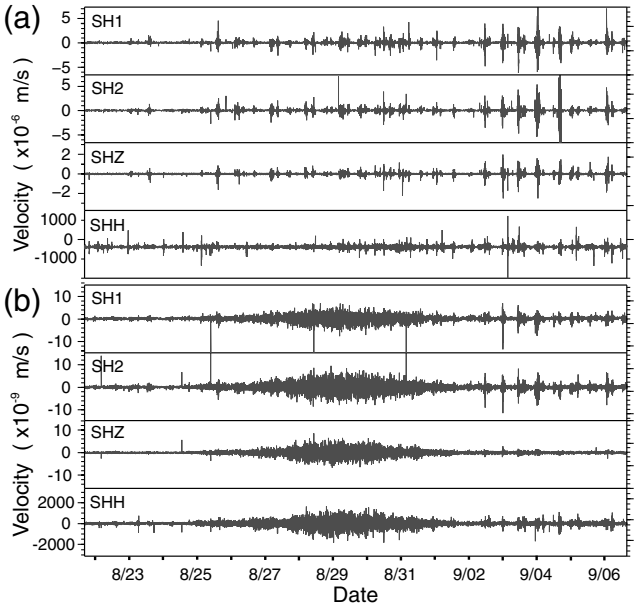

Figure 2. One example of the seismograms recorded by OBS01 (a) without any filtering and (b) with a 1 Hz low-pass filter applied. SHH indicates the hydrophone, and SH1, SH2, and SHZ are the two horizontal components and the vertical component of the geophone, respectively.

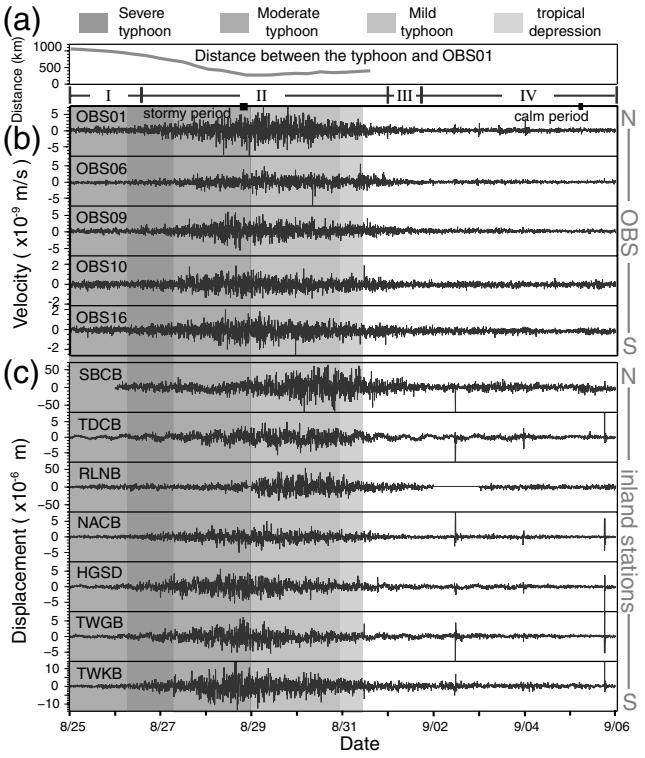

Figure 3. Seismograms recorded at different stations. (a) The distance between OBS01 and the center of the typhoon Nanmadol. Waveform data from the vertical component of the OBSs and some selected inland BATS stations with a 1 Hz low-pass filter applied are shown in (b) and (c). Different typhoon intensities are represented by zones of different shading. The symbols I, II, III, and IV indicate the time windows that we used for the analyses in Figure 7. The two black bars on the top of (b) show the two times that we used to define the stormy period and the calm period.

period from 22 August to 6 September 2011, when the typhoon was near Taiwan (Fig. 2). No significant amplitude change was observed over that time (Fig. 2a). Previous studies suggest that the main energy peak of microseisms affected by ocean activities occurs between approximately 0.05 and 0.5 Hz (Bromirski, 2001). Thus, we applied a 1 Hz low-pass filter to the raw waveform data, and a wave packet appeared for all four components (Fig. 2b). The presence of the wave packet corresponds to the period when the typhoon was passing near Taiwan. The amplitude of the wave packet started increasing 25 August, reaching its maximum during 28 and 29 August, and decreased 2 September. In addition, we also found that the amplitude of the wave packet shows negative correlation with the distance between the OBS and the typhoon (Fig. 3a): the amplitude is the largest when the typhoon is closest to the station. Thus, the typhoon could be the source of the microseism, and the approach of the typhoon could have caused the magnification of the seismic signal. To further understand the relationship between the distance and signal amplitude, the filtered waveform data of the BATS stations were also examined (Fig. 3c). We found that the maximum amplitude appeared earlier in the stations closer to the typhoon center. The amplitude pick for the southernmost stations (TWKB and TWGB) have earlier arrivals than those of OBSs located farther north, although the difference is not very significant. Interestingly, the seismic signals for the stations along the west coast of Taiwan (SBCB and RLNB) showed a visible delay relative to the signals recorded by the stations located on the east coast (NACB, HGSD, TWGB, and TWKB). In addition, the western stations also possess 5–10 times larger signal amplitudes than do the eastern stations (Fig. 3c).

When the typhoon approached, signal magnification was observed in all four components of all the OBSs (Fig. 2b). However, the values of the amplitude magnification of the four components differed. More obvious and stable amplitude changes were observed in the vertical component of the geophones, whereas relatively small and unstable magnification was shown along the two horizontal components. To obtain a more quantitative comparison of the amplification of each component, we used data over two time intervals (the two black bars in Fig. 3a) to calculate the amplification ratio. The first time interval (stormy period) was from 22:30 to 23:30 on 28 August, when the typhoon had the largest effect on Taiwan and the wave packet showed its maximum amplitude. The second time interval (calm period) was from 01:00 to 01:30 on 5 September, when the typhoon had moved far from Taiwan and was classified as a tropical storm, and the wave packet had completely disappeared (Fig. 3). The average amplitudes of the seismograms for the two time periods were calculated, and the value of the amplitude magnification for each component was obtained by dividing the

Table 2
Signal Amplification of the Four Components of Each OBS

Station	Depth (m)	SHH	SHZ	SH1	SH2
OBS01	878.63	6.64	6.91	7.69	8.06
OBS02	1110.90	4.98	8.83	7.79	7.80
OBS03	1234.10	4.36	9.61	1.37	7.61
OBS04	1381.30	4.59	10.16	6.13	7.74
OBS06	1239.60	2.96	6.45	1.13	4.68
OBS07	1036.30	4.33	7.28	4.78	5.07
OBS08	757.77	2.51	2.58	1.21	0.32
OBS09	537.79	3.16	6.08	5.20	1.14
OBS10	2886.30	3.71	3.33	0.99	2.06
OBS11	3018.90	3.22	4.68	4.08	5.16
OBS12	2979.60	4.04	6.55	5.87	1.02
OBS13	2454.20	3.21	5.96	0.36	3.79
OBS14	2353.20	3.40	6.14	1.15	4.45
OBS15	2805.50	3.57	3.34	1.09	3.13
OBS16	3608.20	3.55	4.08	5.79	4.99

average amplitude of the first time period by that of the second time period. After the calculation, the amplitude magnifications for the two horizontal components, vertical component, and hydrophone were estimated to be approximately 0.36–7.79, 0.32–8.06, 2.58–10.16, and 2.51–6.64, respectively (Table 2). This calculation shows that the hydrophone component had the smallest variation in the magnification. Except at OBS01, OBS06, and OBS08, the hydrophone component had a magnification value between 3 and 5. In general, the stations located in the northern profile (OBS01 through OBS07) had larger magnifications (an average of 4.56) than those in the southern profile (OBS10 through OBS16; average 3.53; Table 1). The largest magnification generally appeared in the vertical component of the geophone. The two horizontal components showed variable magnification among the various stations, which was most likely caused by lateral ocean current activity. Because the vertical component showed both the largest magnification by the typhoon and relatively stable variation among stations, we used the data recorded by the vertical component to compose the following discussion.

Frequency Domain

To further study the frequency characteristics of the microseisms caused by the typhoon, we performed a spectral analysis on the waveform data recorded by the OBSs and the inland stations over the period when the typhoon Nanmadol was close to the seismometers (Fig. 4). The elements of the power spectral density (PSD) matrix **P** area are given by $P(i,j) = k|S(i,j)|^2$, in which $S(i,j)$ is the short-time Fourier transform of the input signal and k is a real-valued scalar defined as $k\frac{2}{F_s\Sigma_{n=1}^{L}|w(n)|^2}$. $w(n)$ denotes the window function and F_s is the sampling frequency. In our study, we have resampled our data to have a sampling rate of 1 Hz; a window length of 1024 points shifted in steps of 512 points was used. The spectrogram shows a high-energy signal up to

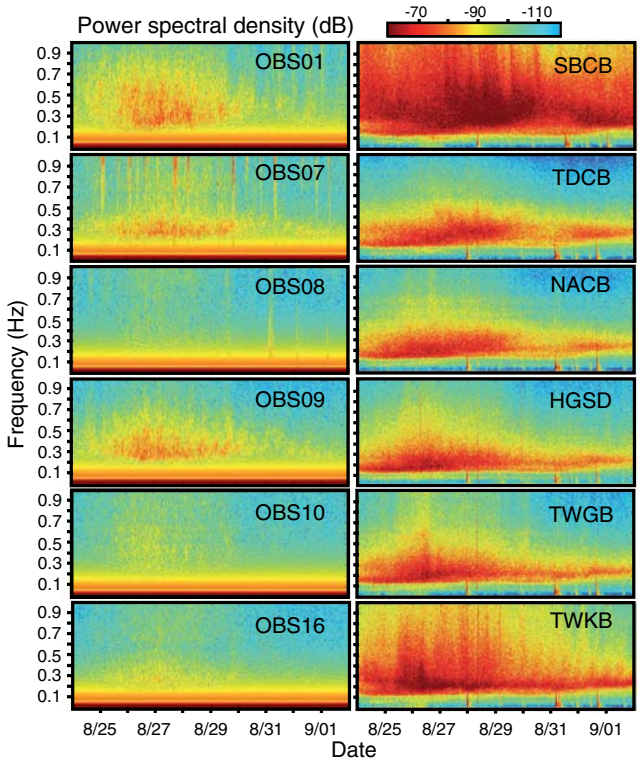

Figure 4. Spectrograms of 10 days of data (24 August to 2 September) recorded by the vertical component of the OBSs and some selected inland BATS stations. The unit of the power spectral density (PSD) dimension for the OBSs and the BATS stations is different: velocity for the former and displacement for the later. The color version of this figure is available only in the electronic edition.

6 days long (from 27 August to 1 September) at all the seismic stations. Much of the energy was concentrated in the 0.15–0.5 Hz frequency range. The signal reached maximum energy on 28 August (Fig. 4) when the typhoon made landfall in Taiwan. The frequency band effected by the typhoon (0.15–0.5 Hz) corresponds to the energy peak of the SPDF events. Thus, the origin of this high-energy signal could be the local sea winds, as suggested by Bromirski *et al.* (2005).

In the previous section, we showed that even though the amplitudes of the 1 Hz low-pass-filtered signal increased at all OBSs when the typhoon was passing, their amplitude magnification was different at each station. Here, we attempt to explain this observation by calculating the PSD between the stormy and calm periods (bars in Fig. 3). To do so, we first extracted the unfiltered waveform data for the stormy and calm periods to calculate their PSD distributions (Fig. 5). We found that when the sea is relatively calm (during the second time segment), the OBSs located along the northern profile had larger PSD values than those along the southern profile, averaging approximately −98 and −104 dB, respectively (Fig. 5c,d). Because the northern stations have generally shallower water depth (shallower than 1400 m) and they recorded relatively higher background noise energies, it appears that the wave energy attenuated with water depth.

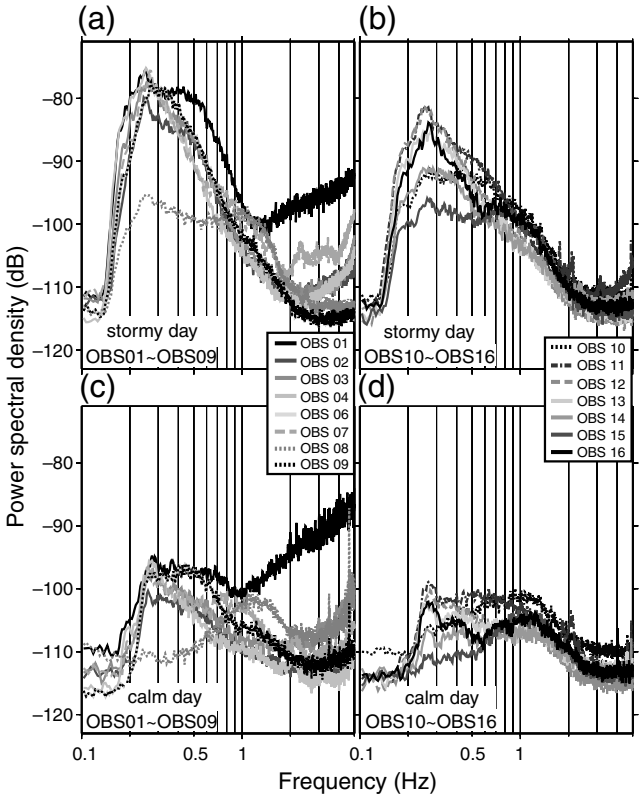

Figure 5. PSD distribution at the various OBSs calculated from the data recorded during the (a and b) stormy and (c and d) calm periods. Lines show the PSD of the different OBS stations. The dB of the PSD unit is from $(m/s)^2/Hz$.

However, the PSD of OBS08 does not fit this observation: low power was observed even though it was deployed in shallow water. Similarly, during the stormy period, PSD curves for stations shallower than 1400 m had, on average, more energy than did the stations deeper than 2300 m (Fig. 5a,b). Finally, a difference of approximately 15–20 dB in PSD values, mainly concentrated at the frequency band of 0.15–0.5 Hz, was observed for almost all the stations between the two periods. The stations in shallower water generally experienced a larger increase in PSD values than did stations in deeper water. However, we notice that this depth-dependent variation was not absolute over small depth ranges. For example, OBS16 had the deepest water depth, but its PSD was not the smallest (Fig. 5b). This observation suggests that factors other than water depth can influence the PSD distribution.

Discussion

Energy Magnification at Different OBS Stations

Even though the signal amplitudes reach their maxima in the frequency band from 0.15 to 0.5 Hz at all the OBSs, the analyses of the amplitude and wave PSD distribution show that the energy changes differ for each OBS. Here, we discuss possible factors for this discrepancy in energy amplification.

First, because the distance between each OBS station is relatively small compared to that between the OBSs network and the typhoon (Fig. 1), all the OBSs can be considered to have a similar position relative to the typhoon. Thus, the distance factor should not be the cause for the variation in signal amplification among the OBSs. Likewise, even though the intensity of the typhoon varied with time, the typhoon strength perceived at each station should not vary with station location. Thus, neither the typhoon intensity nor its distance from the OBSs appears to be the main cause for the differential amplification among the OBSs.

The shallowest and deepest OBSs in our study are located at 534 and 3608 m depths, respectively. With such differences in water depth, we expect that an unequal degree of energy attenuation could occur as a function of depth. To test this idea, we compared the depth of the OBSs (Table 1) and the maximum PSD value (Fig. 5a,b) obtained by each OBS during the passing of the typhoon (Fig. 6a). The regression between the depth of the OBS and the maximum PSD shows a negative correlation, with an R-squared value of 0.159 (correlation coefficient of 0.399). However, we note that OBS08 is located far from the regression curve (Fig. 6a) and thus exclude its data from a second regression, obtaining an R-square value of 0.5004 (correlation coefficient of 0.7074; Fig. 6a). This result suggests that the PSD value may be related to the depth of the station: the deeper the station, the smaller the signal energy. Put another way, the water column attenuates seismic energy.

As described previously, factors other than water depth can influence the PSD distribution. Here, we discuss the possible influence of bad instrument response and different geologic environment on our analyses and explain why water depth is likely the main cause for the discrepancy of amplitude for the seismic records. Regarding the instrument response, a known seismic source has been used to check the instrument response of all the OBSs used in the experiment. The result shows a similar amplitude range for all the instruments, indicating that the instrument response for all the OBSs should be the same. In addition, if the OBS08 had bad instrument response and recorded less energy with respect to other stations, it will be difficult to explain the similar, even higher energy intensity of OBS08 for the frequency larger than 1 Hz as shown in Figure 5a,c. With respect to the site effects, the frequency of the main peak observed in the spectral distribution of seismogram often correlates with the sediment thickness at the site. In our data, the maximal amplitudes of the spectral distribution for all the stations appear in a similar frequency range (about 0.2–0.5 Hz), which suggests that the difference of seismic energy should not result from the site effect. Bringing all the observations together, we conclude that the influence of instrument response and site effect on the signal amplitude may be minor and water depth appears to be the main factor for the variation of seismic energy recorded by the OBSs.

To further understand the reasons for the deviation of OBS08 from the regression curve, we examined the

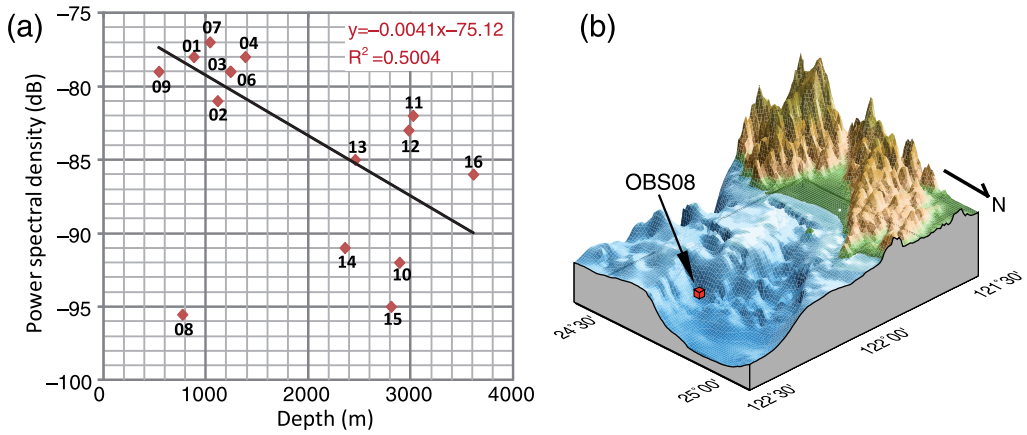

Figure 6. (a) Correlation between the depth of OBSs and their maximal PSD value recorded during the stormy period (shown in Fig. 5a,b). Straight line is the linear regression without the data from OBS08. (b) The 3D bathymetric map around the station OBS08. The cube shows the position of OBS08, showing that the station is located in a bathymetric notch. The dB of the PSD unit is from $(m/s)^2/Hz$. The color version of this figure is available only in the electronic edition.

environmental condition of OBS08. We found that OBS08 was located in a bathymetric notch (Fig. 6b). The high terrain around OBS08 may act as a barrier that prevented the influence of the ocean wave. Further investigation shows that the energy amplification of the hydrophone at OBS08 is much smaller than at other OBSs (Table 1), which indicates that the pressure changes in the water column above OBS08 are smaller than at other stations. As mentioned in several previous studies, pressure changes in the water column can be transmitted to the seafloor as elastic energy that affects the ground motion (Bromirski *et al.*, 2005; Chi *et al.*, 2010; Zhang *et al.*, 2010). Thus, the smaller amplification of the vertical component of OBS08 may result from small pressure changes induced by bathymetric characteristics at OBS08. Consequently, we suggest that the main factor causing OBS08 to be an outlier from the regression curve is the site effect: the pressure changes caused by the ocean waves were damped because OBS08 is protected in a bathymetric notch.

Amplitude Variation at the Inland Stations

As described in the previous section, the waveform data for the stations along the west coast of Taiwan (SBCB and RLNB) show a visibly larger amplitude and time delay than do the signals recorded by the stations located on the east coast (NACB, HGSD, TWGB, and TWKB; Fig. 3c). The wave energy of the west-coast stations started increasing largely after the typhoon passed through Taiwan. When the typhoon's center was located on the east coast, the high mountains in Taiwan may have protected the west coast from the influence of the sustained winds of the storm circle. Thus, little wave activity was generated on the sea surface offshore of the west coast, resulting in the relatively low wave energy recorded by the west-coast stations when the typhoon's center was located on the east coast. Consequently, the time delay of the maximum wave amplitude for the western stations implies that the local sea activity is the main cause of the increase in wave energy during the passing of the typhoon.

In addition, as described previously, the stations along the west coast of Taiwan (SBCB and RLNB) have amplitudes almost 10 times those of the stations located on the east coast (NACB, HGSD, TWGB, and TWKB). Because the TWKB station was located right next to the path of the typhoon (Fig. 1), the energy it recorded is very small compared to that of stations SBCS and RLNB for the frequency range (Figs. 3 and 4). The relative large amplitudes of the stations along the west coast could not only be attributed to the short distance from OBS and the source. Meanwhile, the bathymetry is deeper and the ocean is wider on the east coast of Taiwan than on the west coast. We believe that the amplitude differences for the stations on the two coasts may be caused by the different bathymetric characteristics. The shallow depth or the narrow strait width on the west coast may increase the wave–wave interaction and induce larger wave energy. However, further investigation is required to verify the true origin of this observation.

Tidal Effects

We observed that the energy distribution in the seismograms shows a half-day period change (Fig. 4). This periodic signal was more obvious for the OBSs in shallow water. In addition, the energy in the 0.15–0.5 Hz frequency band increased when the typhoon was passing, also emphasizing the presence of this half-day periodic signal. Tides are the vertical rise and fall of the water; this sea level change may generate pressure variations and affect the microseisms signal. Overlapping the data of the PSD distribution of OBS01 and the data obtained from its closest tide gauge (Longdong; Fig. 7a) shows that the low-tide times correspond well to times of low seismic energy, suggesting that there is a tidal effect on microseismic energy (Fig. 7a).

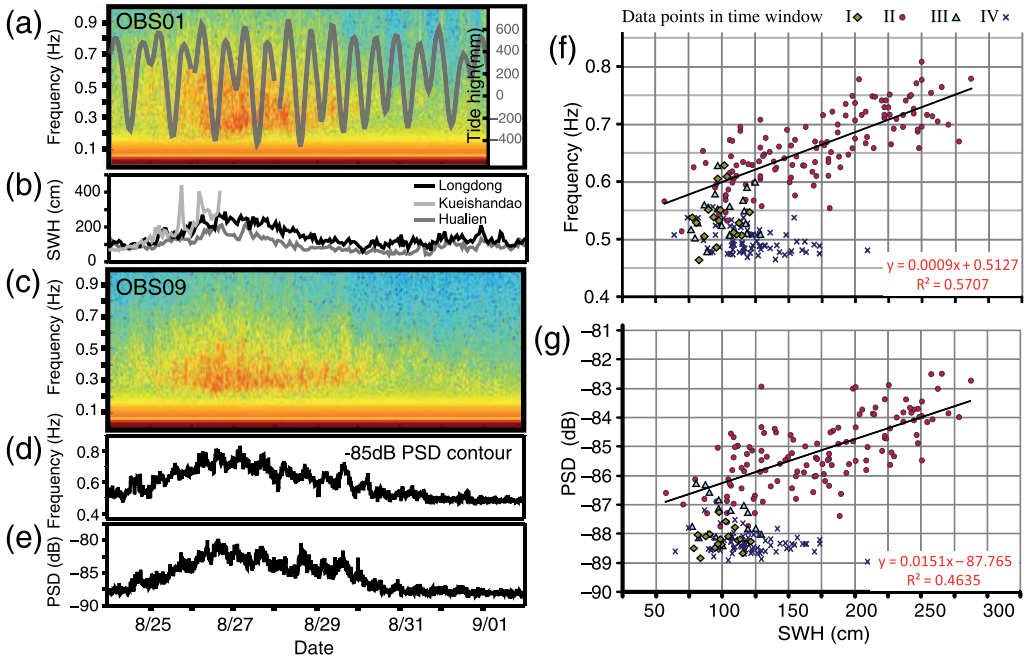

Figure 7. Correlation between the seismic signals recorded by the OBS and the marine meteorological data. Spectrograms of the vertical component of the data recorded by OBS01 and OBS09 are displayed in (a) and (c). (b) Significant wave heights (SWHs) recorded by the Longdong, Kueishantao, and Hualien wave buoys. Line in (b) shows the tide height recorded by the Longdong tide gauge. (d) −85 dB PSD contour of the OBS09 spectrogram shown in (c). (e) PSD value extracted from the OBS09 spectrogram at a frequency of 0.5 Hz. (f) Distribution of SWH and its corresponding frequency when the PSD value is −85 dB. (g) Distribution of SWH and its corresponding PSD value at 0.5 Hz. In (f) and (g), black lines show the regression result, and the regression equations are shown on the figures. The dB of the PSD unit is from $(m/s)^2/Hz$. The color version of this figure is available only in the electronic edition.

Local Wave Height Data

The significant wave heights (SWHs) recorded by the wave buoys show a systematic change during the passing of the typhoon (Fig. 7b). SWH began to increase on 27 August, reached a maximum on 29 August, and then gradually decreased until 1 September. To ensure that the microseismic signal observed in the OBS records is related to the local pressure change produced by the waves, we analyzed the correlation between the seismic energy and SWH. The time evolution of the PSD at 0.5 Hz extracted from the spectrogram of OBS01 (Fig. 7e) was compared with the SWH recorded by the Longdong wave buoy (Fig. 7g). We found that the distribution of the data points varies with time. Thus, we separated the total records into four time windows (I, II, III, and IV in Fig. 3) based on this data distribution. During the period that the typhoon was passing over the OBSs (time window II; points in Fig. 7g), the wave energy and the wave heights show a positive correlation. The wave energy varies from −82 to −88 dB, and the wave height varies from 55 to 285 cm. Regression of the data from time window II yields an *R*-squared of 0.4658 (correlation coefficient of 0.6810; Fig. 7g), suggesting a very high correlation between the wave energy and wave height when the typhoon was passing. No such correlation was observed for the data in the other three time windows. During time windows I and III, when the typhoon was, respectively, approaching and leaving Taiwan, the wave energy alternated between −86 and −89 dB, but few corresponding wave height changes were observed, with wave height varying only from 75 to 125 cm (diamonds and triangles in Fig. 7g). For time window IV, after the typhoon had totally disappeared, a variation of wave height between 60 and 210 cm accompanied a stable wave energy value of approximately −89 to −87 dB (crosses in Fig. 7g).

To understand the relationship between the frequency range and SWH, we extracted the corresponding frequencies of the −85 dB contour from the spectrogram of OBS09 (Fig. 7d) and compared them to the SWH recorded at the Longdong buoy. We observed similar data patterns as observed for the four time windows in the previous analysis. During the passing of the typhoon, the maximum frequency reached by the −85 dB energy contour shows a positive correlation with the wave height, suggesting that the higher the wave, the larger the frequency it can affect. The *R*-squared value of this positive correlation is 0.5707 (correlation coefficient of 0.6810; Fig. 7f). This result suggests that the typhoon may not only increase the energy of the microseism but also may induce higher frequency wave activity during its passing. Previous studies show an increase of the frequency content could be linked to the wave–wave interactions: the high-period ocean waves travel faster than the low-period waves. They hit the coast first, reflected, and interact with the incident waves, which increases the frequency content (Bromirski *et al.*, 2005). Thus, the rise of frequency

during the approach of the typhoon could be explained. To the contrary, just before the landing of the typhoon, the local wind intensifies, which could cause the shift of the energy peak toward the low-frequency domain (Bromirski and Duennebier, 2002).

The data for the time window IV show an interesting pattern: even though the wave height reaches up to 175 cm after the disappearance of typhoon, the frequency remained in the range of 0.45–0.55 Hz. This suggests that the influence of the microseisms in the frequency band of 0.15–0.5 Hz persists even during calm weather and that the wave energy in this frequency band is simply enhanced during the passing of a typhoon.

To explain the increases in wave energy without significant local wave height changes during time windows I and III, we noted that even though the typhoon existed during both time periods, it was located far from our OBS network. Thus, the local sea environment above the OBS network was most likely not effected, as evidenced by the very small wave height changes. However, the *P* waves originating in the deep ocean near the typhoon could be transmitted simultaneously through the rock (Gerstoft *et al.*, 2008; Zhang *et al.*, 2010), which would cause an increase in wave energy in the OBS record. In contrast, the OBS network was located in the periphery of the typhoon during time window II, so the typhoon could induce locally stronger wave activity and generate relatively higher wave energy. This is a good explanation for the highly positive correlation between the wave energy and the wave height observed during time window II. Finally, even though local winds may excite large wave heights during calm periods such as time window IV, very little evidence for this was observed in the wave energy at frequencies between 0.15 and 0.5 Hz, indicating that the enhanced energy of the microseisms cannot be incited simply by nonperiodic sea level changes.

Chi *et al.* (2010) obtained a very high coherence between the pressure and acceleration time series recorded by their OBS when the typhoon was passing. They suggested that the ground motions were mostly responses to pressure sources near the OBS rather than responses to excitations in distant regions. Their result is consistent with what we observed for the data in time window II, when the OBSs are in the typhoon periphery. However, we also see *P*-wave microseisms generated in the deep sea by local sea winds caused by a distant storm before and after the passing of the typhoon. Previous studies suggested that this type of *P*-wave microseism was generated far from the coast in the deep ocean, reflected off of Earth's core, and finally arrived at stations on the other side of the Earth (Gerstoft *et al.*, 2008; Koper and de Foy, 2008; Landès *et al.*, 2010; Zhang *et al.*, 2010). The detailed relationship between this *P*-wave microseism and the local waves was unclear. In our study, we demonstrated that when the OBSs were outside the typhoon periphery, the energy of this *P*-wave microseism was independent of surface-wave activity.

Conclusions

In our study, we used a temporary observation network of 15 OBSs that collected waveform data for approximately 20 days coupled with marine meteorological observation buoys to investigate characteristics of the microseisms induced by the typhoon. The main conclusions are as follows:

1. The energy caused by the typhoon and recorded by the OBS occurs mainly in the frequency band between 0.15 and 0.5 Hz, which corresponds to the SPDF-type microseisms, as suggested by previous studies. The waveform amplitudes are inversely related to the distance between the typhoon and seismometer.
2. The low energy recorded by OBS08 indicates that the site effect is an important factor that influences largely the energy level of microseisms. Besides, the energy of the microseism recorded by the OBSs also varies with different water depth, suggesting that the microseismic energy attenuates with depth. To our knowledge, our study is the first to observe this depth-dependent attenuation of the microseismic signal. The observation was possible because of the variation in water depths of our seismometers.
3. The positive correlation between the wave energy and the local wave height suggests that the microseisms are effected by the pressure changes produced by the local wave activity during the passing of a typhoon. However, in time periods when the OBSs were not located in the typhoon periphery, the wave energy changed without significant variation in wave height. The origin of this energy change was not related to the local wave activity but could be explained instead by the elastic wave formed around the typhoon area, which transmitted through the ocean floor to the stations. This result is important for typhoon monitoring because the increase of microseismic energy before a typhoon passes, even if there are no changes in the local wave height, can provide useful forecasting information.
4. The presence of microseisms in the frequency band from 0.15 to 0.5 Hz persists even during calm weather. In addition, even though local winds can excite large wave heights during calm weather, few show energy in the frequency domain between 0.15 and 0.5 Hz, indicating that the enhanced energy of the microseisms could not be incited simply by such nonperiodic sea level changes.
5. Larger amplitudes were recorded at the stations located along the west coast of Taiwan than at those along the east coast. This may be caused by the different bathymetry in these two places: the west coast is characterized by a narrow and shallow strait, which may increase the wave–wave interaction and increase the energy of the microseisms. This observation could be useful for evaluating seafloor seismometer sites for earthquake detection.

Data and Resources

Seismograms from the OBSs used in this study were collected using a temporary OBS network deployed for the

purpose of the Across Taiwan Strait Explosion Experiment 2011 project and cannot be released publicly. The Broadband Array in Taiwan for Seismology database was searched using bats.earth.sinica.edu.tw (last accessed August 2013). The marine meteorological data were obtained from the Central Weather Bureau of Taiwan (www.cwb.gov.tw/eng; last accessed July 2014). Some information about the typhoon Nanmadol was extracted from the website http://en.wikipedia.org/wiki/Typhoon_Nanmadol_%282011%29 (last accessed July 2014). Most plots were made using Generic Mapping Tools version 4.2.1 (www.soest.hawaii.edu/gmt, last accessed July 2014; Wessel and Smith, 1998). Spectrogram and power spectral density calculations were performed using the software seismic analysis code downloaded from http://www.iris.edu/dms/nodes/dmc/software/downloads/sac (last accessed July 2014) and MATLAB 6 (http://www.iris.edu/dms/nodes/dmc/software/downloads/sac; last accessed July 2014).

Acknowledgments

We thank two anonymous reviewers for their careful reviews, which helped a lot to improve this manuscript. This research was supported by the Taiwan Earthquake Research Center (TEC) and funded through Ministry of Science and Technology with Grant Numbers MOST-103-3113-M-008-001 and MOST-103-2116-M-008-017. The TEC contribution number for this article is 00105.

References

Auffret, Y., P. Pelleau, F. Klingelhoefer, L. Geli, J. Crozon, J. Lin, and J.-C. Sibuet (2004). MicrOBS: A new generation of ocean bottom seismometer, *First Break* **22,** no. 7, 41–47.

Bradley, C., R. Stephen, L. Dorman, and J. Orcutt (1997). Very low frequency (0.2–10.0 Hz) seismoacoustic noise below the seafloor, *J. Geophys. Res.* **102,** no. B6, 11703–11718.

Bretschneider, C. L. (1959). *Wave Variability and Wave Spectra for Wind-Generated Gravity Waves*, Corps of Engineers, Beach Erosion Board, Washington, D.C.

Bromirski, P. D. (2001). Vibrations from the "perfect storm," *Geochem. Geophys. Geosyst.* **2,** no. 7, doi: 10.1029/2000GC000119.

Bromirski, P. D., and F. K. Duennebier (2002). The near-coastal microseism spectrum: Spatial and temporal wave climate relationships, *J. Geophys. Res.* **107,** no. B8, 2166.

Bromirski, P. D., F. K. Duennebier, and R. A. Stephen (2005). Mid-ocean microseisms, *Geochem. Geophys. Geosyst.* **6,** no. 4, Q04009, doi: 10.1029/2004GC000768.

Chi, W.-C., W.-J. Chen, B.-Y. Kuo, and D. Dolenc (2010). Seismic monitoring of western Pacific typhoons, *Mar. Geophys. Res.* **31,** no. 4, 239–251.

Dahm, T., F. Tilmann, and J. Morgan (2006). Seismic broadband ocean-bottom data and noise observed with free-fall stations: Experiences from long-term deployments in the North Atlantic and the Tyrrhenian Sea, *Bull. Seismol. Soc. Am.* **96,** no. 2, 647–664.

Ebeling, C. W., and S. Stein (2011). Seismological identification and characterization of a large hurricane, *Bull. Seismol. Soc. Am.* **101,** no. 1, 399–403.

Gerstoft, P., P. M. Shearer, N. Harmon, and J. Zhang (2008). Global P, PP, and PKP wave microseisms observed from distant storms, *Geophys. Res. Lett.* **35,** L23306, doi: 10.1029/2008GL036111.

Hasselmann, K. (1963). A statistical analysis of the generation of microseisms, *Rev. Geophys.* **1,** no. 2, 177–210.

Kedar, S., and F. H. Webb (2005). The ocean's seismic hum, *Science* **307,** no. 5710, 682–683.

Kibblewhite, A., and C. Wu (1993). Acoustic source levels associated with the nonlinear interactions of ocean waves, *J. Acoust. Soc. Am.* **94,** no. 6, 3358–3378.

Koper, K. D., and B. de Foy (2008). Seasonal anisotropy in short-period seismic noise recorded in South Asia, *Bull. Seismol. Soc. Am.* **98,** no. 6, 3033–3045.

Landès, M., F. Hubans, N. M. Shapiro, A. Paul, and M. Campillo (2010). Origin of deep ocean microseisms by using teleseismic body waves, *J. Geophys. Res.* **115,** no. B05302, doi: 10.1029/2009JB006918.

Longuet-Higgins, M. S. (1950). A theory of the origin of microseisms, *Phil. Trans. Roy. Soc. Lond. A* **243,** no. 857, 1–35.

Marzorati, S., and D. Bindi (2006). Ambient noise levels in north central Italy, *Geochem. Geophys. Geosyst.* **7,** no. 9.

Marzorati, S., and D. Bindi (2008). Characteristics of ambient noise cross correlations in northern Italy within the frequency range of 0.1–0.6 Hz, *Bull. Seismol. Soc. Am.* **98,** no. 3, 1389–1398.

McNamara, D. E., and R. P. Buland (2004). Ambient noise levels in the continental United States, *Bull. Seismol. Soc. Am.* **94,** no. 4, 1517–1527.

Stephen, R. A., F. N. Spiess, J. A. Collins, J. A. Hildebrand, J. A. Orcutt, K. R. Peal, F. Vernon, and F. B. Wooding (2003). Ocean seismic network pilot experiment, *Geochem. Geophys. Geosyst.* **4,** no. 10.

Suda, N., K. Nawa, and Y. Fukao (1998). Earth's background free oscillations, *Science* **279,** no. 5359, 2089–2091.

Sutton, G. H., and N. Barstow (1990). Ocean-bottom ultralow-frequency (ULF) seismo-acoustic ambient noise: 0.002 to 0.4 Hz, *J. Acoust. Soc. Am.* **87,** 2005–2012.

Tabulevich, V. (1971). The effect of the velocity of the centre of a cyclone on the generation of microseisms, *Pure Appl. Geophys.* **85,** no. 1, 69–74.

Webb, S. C. (1998). Broadband seismology and noise under the ocean, *Rev. Geophys.* **36,** no. 1, 105–142.

Webb, S. C. (2007). The Earth's 'hum' is driven by ocean waves over the continental shelves, *Nature* **445,** no. 7129, 754–756.

Wessel, P., and W. H. F. Smith (1998). New, improved version of generic mapping tools released, *Eos Trans. AGU* **79,** no. 47, 579, doi: 10.1029/98EO00426.

Wilson, D. K., G. V. Frisk, T. E. Lindstrom, and C. J. Sellers (2003). Measurement and prediction of ultralow frequency ocean ambient noise off the eastern US coast, *J. Acoust. Soc. Am.* **113,** 3117.

Zhang, J., P. Gerstoft, and P. D. Bromirski (2010). Pelagic and coastal sources of *P*-wave microseisms: Generation under tropical cyclones, *Geophys. Res. Lett.* **37,** no. 15, L15301, doi: 10.1029/2010GL044288.

Department of Earth Sciences and Institute of Geophysics
National Central University
300 Jhongda Road
Jhongli City
Taoyuan County 32001, Taiwan
jylin@ncu.edu.tw
jylin.gep@gmail.com
lee_chuan_chuan@hotmail.com
letyougoster@gmail.com
changpukong@gmail.com
ray265@gmail.com
sharon000095@hotmail.com
(J.-Y.L., T.-C.L., H.-S.H., Y.-F.C., Y.-C.L., H.-H.L.)

Department of Earth and Environment Sciences
National Chung Cheng University
No. 168, Sec. 1, University Rd.
Min-Hsiung Township
Chia-yi County 621, Taiwan
yiyingwen@gmail.com
(Y.-Y.W.)

Manuscript received 5 September 2013;
Published Online 16 September 2014